Mechanics of fault reactivation before, during, and after the 2015 eruption of Axial Seamount

Article *in* Geology · March 2018

DOI: 10.1130/G39978.1

CITATIONS
19

READS
286

7 authors, including:

Samuel Levy
North Carolina State University
2 PUBLICATIONS **46** CITATIONS
SEE PROFILE

D. R. Bohnenstiehl
North Carolina State University
189 PUBLICATIONS **3,388** CITATIONS
SEE PROFILE

D. Parker Sprinkle
Pacific Northwest National Laboratory
6 PUBLICATIONS **27** CITATIONS
SEE PROFILE

Margaret S. Boettcher
University of New Hampshire
54 PUBLICATIONS **1,243** CITATIONS
SEE PROFILE

THE GEOLOGICAL SOCIETY OF AMERICA®

Mechanics of fault reactivation before, during, and after the 2015 eruption of Axial Seamount

S. Levy[1], D.R Bohnenstiehl[1], P. Sprinkle[1], M.S. Boettcher[2], W.S.D. Wilcock[3], M. Tolstoy[4], and F. Waldhauser[4]
[1]Department of Marine, Earth & Atmospheric Sciences, North Carolina State University, Raleigh, North Carolina 27695, USA
[2]Department of Earth Sciences, University of New Hampshire, Durham, New Hampshire 03824, USA
[3]School of Oceanography, University of Washington, Seattle, Washington 98195, USA
[4]Lamont-Doherty Earth Observatory of Columbia University, Palisades, New York 10964, USA

ABSTRACT

Ocean-bottom seismic and seafloor pressure data from the Ocean Observatories Initiative's Cabled Array were used to study fault reactivation within Axial Seamount (offshore Oregon, USA). Microearthquakes that occurred during 2015–2016 were located on portions of an outward-dipping ring fault system that was reactivated in response to the inflation and deflation of the underlying magma chamber. Prior to an eruption in April 2015, focal mechanisms showed a pattern of normal slip consistent with the differential vertical uplift of the caldera floor relative to the rim. During the eruption, seismic activity remained localized along these outward-dipping structures; however, the slip direction was reversed as the caldera floor subsided. After the eruption, as the volcano reinflated and the caldera floor uplifted, these faults exhibited sparser seismicity with a more heterogeneous pattern of slip. Monitoring the evolution of ring fault behavior through time may have utility as a metric in future eruption forecasts.

INTRODUCTION

At active volcanoes, as magma is withdrawn from a chamber during an eruption, faults commonly form in response to the subsidence and collapse of the overlying material—developing as either inward-dipping (normal) or outward-dipping (reverse) structures, depending on the amount of subsidence, geometry of the magma chamber, and tectonic setting (Cole et al., 2005; Holohan et al., 2005; Acocella, 2007; Martí et al., 2008). These collapse structures often exhibit a circular to elliptical pattern in plan view and are commonly referred to as ring faults. Reactivation of ring faults has been documented in regional earthquakes studies (e.g., Nettles and Ekström, 1998; Shuler et al., 2013; Gudmundsson et al., 2016); however, the mechanical role of these structures during different phases of the volcanic cycle remains poorly understood.

Axial Seamount is a basaltic shield volcano located at the intersection of the Cobb-Eickelberg hotspot and Juan de Fuca Ridge (offshore Oregon, USA; intermediate spreading rate of 55–60 mm/yr). The summit hosts a caldera at 1500 m below sea level (bsl) that is an elongate depression ~3 km wide and 8.5 km long, with walls up to ~150 m high that are buried by younger lavas to the south (Fig. 1). Multichannel seismic reflection studies have imaged a 3-km-wide by 14-km-long magma chamber offset slightly to the east of the caldera at a depth of 1.1–2.3 km beneath the caldera floor (Arnulf et al., 2014).

Volume-predictable eruptive behavior has been proposed based on bottom-pressure recorder (BPR) studies that have tracked the inflation and deflation of Axial Seamount for nearly two decades, capturing diking events in 1998, 2011, and 2015 (Chadwick al., 2012; Nooner and Chadwick, 2016). Seismicity associated with the 1998 and 2011 eruptions was recorded by regional hydrophone arrays (Dziak and Fox, 1999) and by ocean bottom hydrophones (Dziak et al., 2012), respectively. Following the 1998 eruption, temporary arrays of 4–10 ocean bottom seismometers (OBSs) monitored local seismicity for 15 mo (Sohn et al., 2004). During the 1998 and 2011 eruptions, point-source elastic deformation models indicate that the volume of the magma reservoir decreased by ~0.21 km^3 and ~0.15 km^3, as dikes propagated 55 km and 33 km, respectively, along the southern rift zone (Chadwick et al., 2012).

The most recent eruption at Axial Seamount began on 24 April 2015 and was recorded by a seven-station network of three-component OBSs installed within the caldera as part of the Ocean Observatories Initiative (OOI; http://oceanobservatories.org; Kelley et al., 2014). A dike propagated northward from the eastern margin of the magma chamber, erupting a series of lava flows extending from the northeast caldera floor along the north rift zone up to ~14 km north of the caldera (Chadwick et al., 2016). Seafloor explosions associated with the emplacement of these flows indicate that the 2015 eruption persisted over a period of ~26 d (Wilcock et al., 2016), during which time the volume of the magma reservoir (modeled as a prolate spheroid) decreased by ~0.29 km^3 (Nooner and Chadwick, 2016). During the time period immediately surrounding the eruption (January–September 2015), Wilcock et al. (2016) identified two steeply dipping, outward-facing planes of microearthquakes beneath the southern portion of the caldera. These structures were interpreted to represent portions of a ring fault system reactivated in response to the inflation and deflation of the magma chamber.

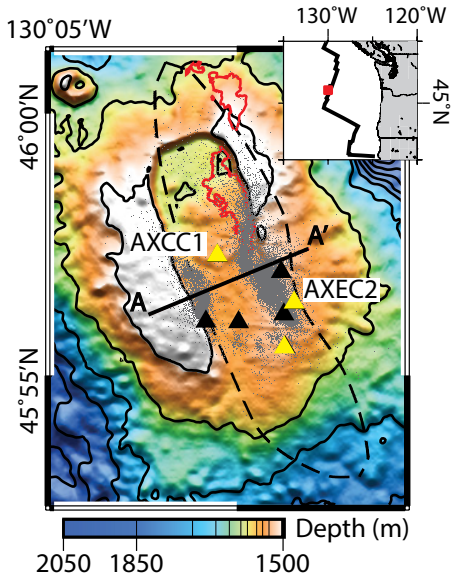

Figure 1. Bathymetry of Axial Seamount (offshore Oregon, USA) with earthquake locations (gray dots), seismic stations (triangles), and collocated bottom pressure recorders (yellow triangles, AXCC1 and AXEC2). Boundary of 2015 lava flows is outlined in red (Chadwick et al., 2016), along with margins of seismically imaged magma chamber (dashed; Arnulf et al., 2014). Profile A-A′ indicates cross section shown on Figure 2. Inset shows regional location.

In this study, we created an independent catalog of microearthquakes (median M_w ~1.0) for a longer time period between January 2015 and December 2016. These data confirmed the proposed fault geometry and allowed us to track changes in fault slip direction over a nearly 2 yr period. OBS data were used to generate a time series of composite focal mechanism solutions

for ring fault earthquakes. This information was used along with the uplift and subsidence history of the caldera, as monitored by the BPRs, to characterize the mechanical behavior of these faults during different phases of the volcanic cycle.

DATA AND METHODS

Using the three-component seismic data from the OOI Cabled Array, primary (P) and secondary (S) phase arrivals were detected automatically using short-term to long-term amplitude ratio and kurtosis metrics (e.g., Baillard et al., 2014), and these were associated to form a set of 41,522 earthquake origins (see the GSA Data Repository[1]). Catalog phase data were then used to relocate hypocenters relative to one another using the hypoDD algorithm (http://www.ldeo.columbia.edu/~felixw/hypoDD.html; Waldhauser and Ellsworth, 2000), yielding a set of 19,049 earthquakes with ≥9 defining phases (see the Data Repository). Seismic moments were estimated from the long-period spectral displacement (Brune, 1970) and summed to constrain the cumulative seismic slip using the scalar seismic moment equation (see the Data Repository), assuming a shear modulus for the upper volcanic crust within the 1–4 GPa range (Gudmundsson et al., 2016).

First-motion polarities and S/P amplitude data were used to generate a total of 100 focal mechanism solutions using the HASH software program (https://earthquake.usgs.gov/research/software/#HASH; Hardebeck and Shearer, 2003). Each solution was formed from a composite of 3–9 events, selected based on the similarity of their vertical channel waveform arrivals (see the Data Repository). Focal mechanisms were classified based on rake as normal (–90° ± 30°), reverse (90° ± 30°), strike-slip (0° or 180° ± 30°), or oblique-normal/reverse. A binomial test was used to determine if the number of normal (or reverse) mechanisms within a given time window was significantly different than expected by a random model.

Data from three BPR stations deployed as part of the OOI Cabled Array (Fig. 1) were processed to remove tidal signals and then converted to estimates of seafloor elevation (see the Data Repository). The differential vertical motion between BPR station AXCC1, on the central caldera floor, and station AXEC2, on the eastern caldera rim (Fig. 1), was calculated during each phase of the volcanic cycle and used to constrain the direction and relative amount of motion expected across the eastern ring fault.

RESULTS

Microearthquake hypocenters were located primarily within the OOI array along the eastern and western margins of the south-central caldera, with the majority of seismicity to the east (Fig. 1). In cross section, relocated hypocenters defined two outward-dipping bands that were fit by planes oriented 330° ± 1°/67° ± 1°E (strike/dip) and 342° ± 1°/66° ± 1°W, respectively. These bands extended from near the margins of the magma chamber at depth and projected onto the seafloor inward of the caldera rim (Figs. 1 and 2). The spatial distribution of microearthquakes remained localized within these outward-dipping structures before, during, and after the 2015 eruption (Wilcock et al., 2016); however, as discussed below, the rate of seismicity and sense of slip changed between these parts of the volcanic cycle.

As the magma chamber inflated leading up to the eruption (January to 23 April 2015), the seafloor rose at a rate of 61 cm/yr near the center

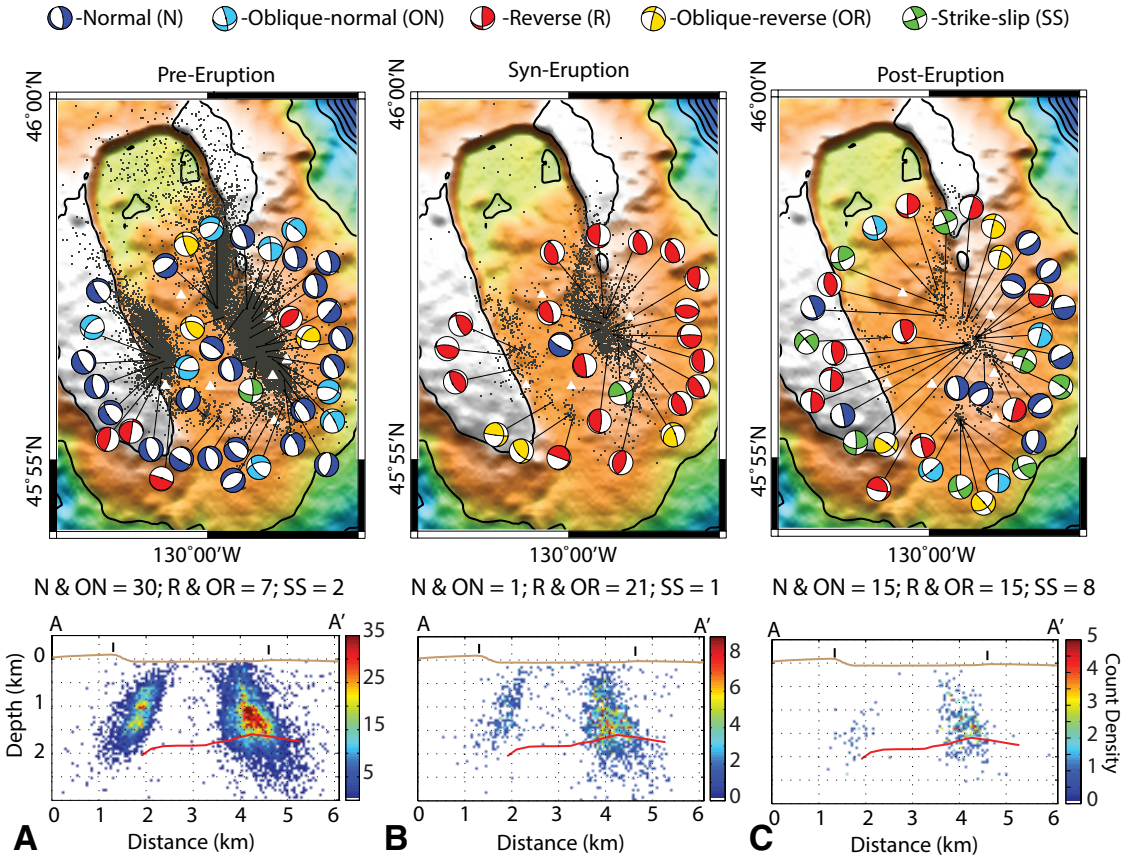

Figure 2. Composite focal mechanism solutions and seismicity (A) before, (B) during, and (C) after 2015 eruption. Shading indicates focal mechanism type. Cross sections show earthquake density (50 × 50 m bins) using hypocenters within 1 km of line A-A′ (Fig. 1). Black ticks delineate location of caldera rim within bathymetry; red line delineates top of magma chamber identified by Arnulf et al. (2014).

[1]GSA Data Repository item 2018138, data and methods for earthquake location procedures, composite focal mechanisms, analysis of bottom pressure data, and seismic moments and cumulative slip estimates, is available online at http://www.geosociety.org/datarepository/2018/ or on request from editing@geosociety.org. Data used for this study are archived at the IRIS Data Management Center (https://ds.iris.edu/ds/nodes/dmc/) and the National Science Foundation Ocean Observatories Initiative Data Portal (http://oceanobservatories.org/data-portal/).

of the caldera (station AXCC1) and 21 cm/yr along its eastern rim (AXEC2). During this time period, on average, 398 microearthquakes were located each day within our catalog. Composite focal mechanisms were determined for 39 microearthquake clusters. The outward-dipping nodal planes for these mechanisms had an average strike of 333° ± 21° and an average dip of 67° ± 4°. The majority (79%) of the mechanisms showed normal (23) or oblique-normal (8) sense of motion (Fig. 2A), with $p < 0.01$ (binomial test) showing statistical significance. The remaining eight focal mechanisms showed one strike-slip and seven reverse/oblique-reverse motions.

Subsidence of the caldera floor began at ~06:00 h UTC on 24 April 2015, marking the initiation of diking and the removal of magma from the chamber (Nooner and Chadwick, 2016; Wilcock et al., 2016). During the subsequent 26 d, maximum subsidence of ~2.5 m (Fig. 3) was recorded at the center of the caldera (AXCC1), with ~1.1 m observed along the eastern rim (AXEC2). Most of this subsidence occurred during the first day of the eruption and was accompanied by an intense period of microearthquake activity (3662 per day) localized along the fault structures (Fig. 2B). The outward-dipping nodal planes for the 23 focal solutions obtained within this 26 d time period had an average strike of 338° ± 16° and an average dip of 69° ± 5°, with a predominantly (91%) reverse (18) and oblique-reverse (3) sense of slip ($p < 0.01$).

After the end of eruptive activity, posteruption uplift of the caldera floor and rim began on approximately 19 May 2015, with average uplift rates of 92 cm/yr (AXCC1) and 29 cm/yr (AXEC2) observed over the next 7 mo (Fig. 3). Beginning in December 2015, the uplift rates decreased by ~50%. By the end of 2016, the caldera-center station AXCCI had recovered 93 cm in elevation. Despite uplift rates that were similar to those during the period leading up to the eruption, the cataloged seismicity rate during this time was very low (<2 earthquakes/d). Composite focal mechanisms generated during this 19 mo posteruptive period exhibited a variable sense of slip, with 15 normal/oblique-normal ($p = 0.26$), 15 reverse/oblique-reverse ($p = 0.26$), and 8 strike-slip events ($p = 0.07$; Fig. 2C). Outward-dipping nodal planes were characterized by an average strike of 007° ± 27° and an average dip of 75° ± 4°.

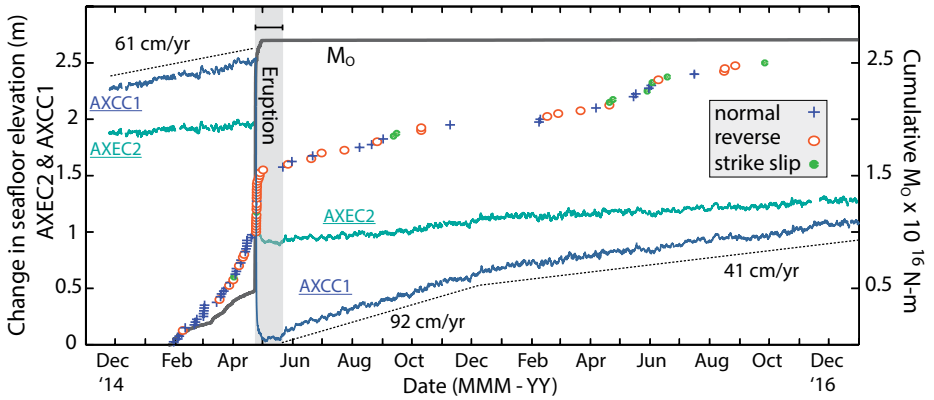

Figure 3. Seafloor elevation changes measured at bottom pressure recorder stations AXCC1 (blue) and AXEC2 (green) overlain with plots of cumulative seismic moment release (black) and focal mechanism solution type (symbols) displayed cumulatively: normal/oblique normal (blue crosses), reverse/oblique-reverse (red circles), and strike-slip (green dots). Symbols show sense of slip for each composite focal mechanism with respect to time.

DISCUSSION

The spatial pattern of hypocenters before, during, and after the 2015 eruption is consistent with activation of a preexisting outward-dipping fault system formed earlier in the volcano's history (e.g., Clague et al., 2013). Earthquakes along the eastern side of the caldera accounted for ~86% of the total seismic moment release. As the completeness level of the seismic catalog is similar (within 0.1–0.2 magnitude units) along the eastern and western margins of the array, this is not likely to be due to OBS station placement. Rather, this pattern may arise due to localized magma replenishment and withdrawal, with recent diking events in 1998, 2001, and 2015 all sourced along the eastern margin of the chamber (Chadwick et al., 2016)—near the modeled source volume of the 2015 eruption (Nooner and Chadwick, 2016), and where melt was observed at shallow depths in multichannel seismic surveys (Arnulf et al., 2014; see Figs. 2 and 4).

In the 3 mo leading up to the 2015 eruption, there was 0.16 m of relative uplift between the caldera center (AXCC1) and eastern rim (AXEC2), which may have been due to some combination of elastic and inelastic deformation. This motion was associated with a period of normal and oblique-normal slip (31 of 39 solutions) along the outward-dipping fault system, with a cumulative dip-slip movement of 0.08–0.30 m (Fig. 4A) along the eastern fault ($\Sigma M_o = 1.66 \times 10^{15}$ N-m was used to solve for slip; see the Data Repository). During dike emplacement and eruption, the caldera center moved downward 1.43 m relative to the eastern rim (Fig. 4B). Focal mechanisms show a dominant pattern of reverse and oblique-reverse motion (21 of 23 solutions) along the fault systems, with a cumulative dip-slip movement of 0.44–1.75 m along the eastern fault ($\Sigma M_o = 9.1 \times 10^{15}$ N-m). The seismic strain and the sense of slip are therefore tightly coupled with the pattern of uplift and subsidence in the months before and during the eruption. Because fault movements can significantly impact volcano deformation models (Folch and Gottsmann, 2006), future efforts to constrain the inflation and deflation of the magma chamber (e.g., Nooner and Chadwick, 2016) should incorporate seismic estimates of fault slip.

During the 19 mo period following the eruption, the caldera center moved upward 0.61 m relative to the eastern rim, with a rate of inflation comparable to that observed prior to eruption. The posteruption seismicity, however, showed a heterogeneous sense of slip and accounted for <0.005 m of motion along the eastern ring fault ($\Sigma M_o = 1.40 \times 10^{13}$ N-m; Fig. 4C). A similarly low rate of moment release was reported during the 15 mo period following the 1998 eruption (Sohn et al., 2004). This implies either that the ring faults

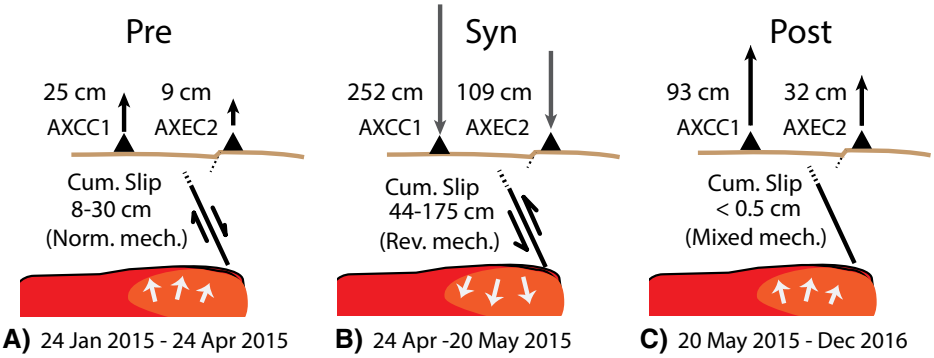

Figure 4. Cartoon showing differential uplift across eastern ring fault and cumulative (Cum.) fault slip during (A) inflation, (B) deflation, and (C) reinflation of magma chamber. Black triangles represent bottom pressure recorder stations. Drawings are not to scale. Norm.—normal; Rev.—reverse.

were able to slide aseismically during these early reinflationary phases, or that these structures remained locked due to a net increase in fault-normal stress associated with the co-eruptive deflation. The latter interpretation is consistent with the sensitivity of ring fault microearthquakes to ocean tidal loading (Tolstoy et al., 2002; Wilcock et al., 2016), which implies they are frictionally strong. These faults, however, are expected to transition to a more seismically active phase as reinflation continues leading up to the next eruption. Single-event (noncomposite) focal mechanisms after the 1998 eruption indicate 15 normal and 6 reverse-slip events (Sohn et al., 2004), suggesting a somewhat more homogeneous pattern of stress compared to the 2015–2016 posteruption period. Such differences could indicate variability in the spatial pattern of magma recharge and/or differences in the residual dike-related thermal and mechanical stresses acting on the structurally complex ring fault system.

CONCLUSIONS

At Axial Seamount, seismic strain is tightly coupled to the volcanic cycle during the later stages of inflation, when portions of the outward-dipping ring fault system are activated with a normal sense of slip, and during deflation, when the motion on these same faults is reversed. Following an eruption, even as uplift rates rival those observed in the later stages of inflation, little to no seismic slip is observed for a period of months to years. Leading up to the next eruption, the cyclic pattern of volcanic deformation will eventually lead to increased seismic moment release (e.g., Tolstoy et al., 2002; Dziak et al., 2012; Wilcock et al., 2016) as the ring fault is again activated with a predominantly normal sense of motion. With the installation of the OOI Cabled Array, the mechanical behavior of the ring faults can be tracked in near real time, and this behavior may provide an additional metric for forecasting future eruptions.

ACKNOWLEDGMENTS

This work was supported under National Science Foundation grants OCE-1536219, OCE-1536320, OCE-1635276, and OCE-1635325. We thank B. Chadwick, J. Gottsmann, S. Nooner, K. Wegmann, and P. Byrne for insightful discussions regarding this manuscript.

REFERENCES CITED

Acocella, V., 2007, Understanding caldera structure and development: An overview of analogue models compared to natural calderas: Earth-Science Reviews, v. 85, p. 125–160, https://doi.org/10.1016/j.earscirev.2007.08.004.

Arnulf, A.F., Harding, A.J., Kent, G.M., Carbotte, S.M., Canales, J.P., and Nedimović, M.R., 2014, Anatomy of an active submarine volcano: Geology, v. 42, p. 655–658, https://doi.org/10.1130/G35629.1.

Baillard, C., Crawford, W.C., Ballu, V., Hibert, C., and Mangeney, A., 2014, An automatic kurtosis-based P- and S-phase picker designed for local seismic networks: Bulletin of the Seismological Society of America, v. 104, p. 394–409, https://doi.org/10.1785/0120120347.

Brune, J.N., 1970, Tectonic stress and the spectra of seismic shear waves from earthquakes: Journal of Geophysical Research, v. 75, p. 4997–5009, https://doi.org/10.1029/JB075i026p04997.

Chadwick, W.W., Nooner, S.L., Butterfield, D.A., and Lilley, M.D., 2012, Seafloor deformation and forecasts of the April 2011 eruption at Axial Seamount: Nature Geoscience, v. 5, p. 474–477, https://doi.org/10.1038/ngeo1464.

Chadwick, W.W., Paduan, J.B., Clague, D.A., Dreyer, B.M., Merle, S.G., Bobbitt, A.M., Caress, D.W., Philip, B.T., Kelley, D.S., and Nooner, S.L., 2016, Voluminous eruption from a zoned magma body after an increase in supply rate at Axial Seamount: Geophysical Research Letters, v. 43, p. 12,063–12,070, https://doi.org/10.1002/2016GL071327.

Clague, D.A., et al., 2013, Geologic history of the summit of Axial Seamount, Juan de Fuca Ridge: Geochemistry Geophysics Geosystems, v. 14, p. 4403–4443, https://doi.org/10.1002/ggge.20240.

Cole, J.W., Milner, D.M., and Spinks, K.D., 2005, Calderas and caldera structures: A review: Earth-Science Reviews, v. 69, p. 1–26, https://doi.org/10.1016/j.earscirev.2004.06.004.

Dziak, R.P., and Fox, C.G., 1999, The January 1998 earthquake swarm at Axial Volcano, Juan de Fuca Ridge: Hydroacoustic evidence of seafloor volcanic activity: Geophysical Research Letters, v. 26, p. 3429–3432, https://doi.org/10.1029/1999GL002332.

Dziak, R.P., Haxel, J.H., Bohnenstiehl, D.R., Chadwick, W.W., Nooner, S.L., Fowler, M.J., Matsumoto, H., and Butterfield, D.A., 2012, Seismic precursors and magma ascent before the April 2011 eruption at Axial Seamount: Nature Geoscience, v. 5, p. 478–482, https://doi.org/10.1038/ngeo1490.

Folch, A., and Gottsmann, J., 2006, Faults and ground uplift at active calderas, *in* Troise, C., et al., eds., Mechanisms of Activity and Unrest at Large Calderas: Geological Society of London Special Publication 269, p. 109–120, https://doi.org/10.1144/GSL.SP.2006.269.01.07.

Gudmundsson, M.T., et al., 2016, Gradual caldera collapse at Bárdarbunga volcano, Iceland, regulated by lateral magma outflow: Science, v. 353, p. 1–24, https://doi.org/10.1126/science.aaf8988.

Hardebeck, J.L., and Shearer, P.M., 2003, Using S/P amplitude ratios to constrain the focal mechanisms of small earthquakes: Bulletin of the Seismological Society of America, v. 93, p. 2434–2444, https://doi.org/10.1785/0120020236.

Holohan, E.P., Troll, V.R., Walter, T.R., Münn, S., McDonnell, S., and Shipton, Z.K., 2005, Elliptical calderas in active tectonic settings: An experimental approach: Journal of Volcanology and Geothermal Research, v. 144, p. 119–136, https://doi.org/10.1016/j.jvolgeores.2004.11.020.

Kelley, D.S., Delaney, J.R., and Juniper, S.K., 2014, Establishing a new era of submarine volcanic observatories: Cabling Axial Seamount and the Endeavour Segment of the Juan de Fuca Ridge: Marine Geology, v. 352, p. 426–450, https://doi.org/10.1016/j.margeo.2014.03.010.

Martí, J., Geyer, A., Folch, A., and Gottsmann, J., 2008, A review on collapse caldera modeling: Developments in Volcanology, v. 10, p. 233–283, https://doi.org/10.1016/S1871-644X(07)00006-X.

Nettles, M., and Ekström, G., 1998, Faulting mechanism of anomalous earthquakes near Bárdarbunga Volcano, Iceland: Journal of Geophysical Research, v. 103, p. 17,973–17,983, https://doi.org/10.1029/98JB01392.

Nooner, S.L., and Chadwick, W.W., 2016, Inflation-predictable behavior and co-eruption deformation at Axial Seamount: Science, v. 354, p. 1399–1403, https://doi.org/10.1126/science.aah4666.

Shuler, A., Nettles, M., and Ekström, G., 2013, Global observation of vertical-CLVD earthquakes at active volcanoes: Journal of Geophysical Research, v. 118, p. 138–164, https://doi.org/10.1029/2012JB009721.

Sohn, R.A., Barclay, A.H., and Webb, S.C., 2004, Microearthquake patterns following the 1998 eruption of Axial Volcano, Juan de Fuca Ridge: Mechanical relaxation and thermal strain: Journal of Geophysical Research, v. 109, B01101, https://doi.org/10.1029/2003JB002499.

Tolstoy, M., Vernon, F.L., Orcutt, J.A., and Wyatt, F.K., 2002, Breathing of the seafloor: Tidal correlations of seismicity at Axial volcano: Geology, v. 30, p. 503–506, https://doi.org/10.1130/0091-7613(2002)030<0503:BOTSTC>2.0.CO;2.

Waldhauser, F., and Ellsworth, W.L., 2000, A double-difference earthquake location algorithm: Method and application to the Northern Hayward fault, California: Bulletin of the Seismological Society of America, v. 90, p. 1353–1368, https://doi.org/10.1785/0120000006.

Wilcock, W.S.D., Tolstoy, M., Waldhauser, F., Gracia, C., Tan, Y.J., Bohnenstiehl, D.R., Caplan-Auerbach, J., Dziak, R.P., Arnulf, A.F., and Mann, E.M., 2016, Seismic constraints on caldera dynamics from the 2015 Axial Seamount eruption: Science, v. 354, p. 1395–1399, https://doi.org/10.1126/science.aah5563.

Manuscript received 8 December 2017
Revised manuscript received 9 February 2018
Manuscript accepted 14 February 2018

Printed in USA